Temperature-insensitive Fast Anion Intercalation Kinetics in Graphite Electrodes for Aluminum-ion Batteries

Shubham Agrawal[1]*, Nick Matteucci*[1,2]*, Bingyuan Ma*[1]*, Jiayi Wu*[1]*, Rochit Sinha*[1,†]*, and Peng Bai*[1,3,]*

[1]Department of Energy, Environmental & Chemical Engineering, Washington University in St. Louis, St. Louis, Missouri – 63130, United States

[2]Department of Chemical Engineering, Massachusetts Institute of Technology, Cambridge, Massachusetts – 02139, United States

[3]Institue of Materials Science and Engineering, Washington University in St. Louis, St. Louis, Missouri – 63130, United States

[†]Present address: Department of Chemical & Biological Engineering, Northwestern University, Evanston, Illinois – 60208, United States

*Email: pbai@wustl.edu

Abstract

Lithium-ion batteries (LIBs) rule today's energy storage market owing to their overall high performance, which, however, deteriorate severely at temperatures below -10°C. Emerging aluminum-ion batteries (AIBs), unlike LIBs, can deliver higher reversible capacities at low temperatures down to even -30°C. Here, we perform a systematic electrochemical characterization of the AIBs using classical electroanalytical methods at five temperatures selected between -20°C and room temperature, to assess the fundamental kinetics. With a generalized model, we obtained diffusion coefficients in the range of $10^{-9} – 10^{-7}\ cm^2\ s^{-1}$, and the rate-limiting mechanism shifts from mixed-control at room temperature to diffusion-control at -20°C. Further independent impedance analysis reveals a much less severe increase in the impedance in AIBs than those in LIBs, at low temperatures. The temperature-insensitive fast kinetics can be attributed to the high availability and easy access of active species at the inner Helmholtz plane near the electrode surface. The results here shed light on the governing mechanisms facilitating the high performance of AIBs in a wide temperature range and demonstrate the necessity of electrolyte optimization with a focus on the inner Helmholtz plane of the electric double layer structure to ensure high-rate electrode performance at low temperatures.

Keywords:

Aluminum-ion battery, Ionic liquid, Reaction kinetics, Electroanalytical techniques, Electrical double layer

1. Introduction

Efficient electrical energy conversion and storage systems are increasingly needed to fulfill future energy demands.[1–3] Lithium-ion batteries (LIBs), while being the most mature portable power sources for both small-scale and large-scale applications, are evolving to become cost-effective, reliably safe, and environmentally friendly. LIBs are known to suffer from quick performance deterioration at low temperatures. At temperatures below -10°C, LIBs are prone to lithium plating on graphite anodes, raising the unpredictable high risk of fire and explosion.[4,5] The compromised performance at low temperatures has been attributed to the following factors: (i) lower ionic conductivity of the electrolyte, (ii) reduced Li-ion diffusion into graphite electrodes, and (iii) significantly increased charge-transfer resistance at the electrode|electrolyte interface with complications from the solid-electrolyte interphase (SEI).[6] Unlike LIBs, aluminum-ion batteries (AIBs), enabled by room-temperature ionic liquid electrolytes, exhibit remarkable high-rate cycling performance at temperatures as low as -30°C, making them an attractive option for cold-weather conditions.[7] The aluminum metal anode also appears particularly promising, owing to its low cost, rich abundance, and processing safety.[8–11] To the best of our knowledge, systematic investigations of the electrochemical kinetics in this AIB system, other than the ionic conductivity of the electrolyte, are yet to be performed to achieve a comprehensive understanding of the coupled interfacial charge transfer and bulk phase transformation dynamics.

Carbon materials, such as natural graphite,[12] amorphous carbon,[13] and graphene microflakes composites,[14] have been successfully demonstrated as a host for the reversible intercalation of the chloroaluminate ($AlCl_4^-$) ions. At room temperature, the Al vs. graphite system with the aluminum chloride:1-ethyl-3-methylimidazolium ($AlCl_3$:[EMIm]Cl = 1.7:1 mole ratio) ionic liquid electrolyte can provide a reversible capacity of 80 mAh g^{-1} at 1C rate with an average cell voltage of 2V.[7] At temperatures lower than -10 °C, not only could the system still function, it even provides a higher capacity due to the emergence of the third intercalation voltage plateau,[7] yet at relatively high C-rates. This phenomenon is in stark contrast to the sluggish Li intercalation into graphite electrodes, given that the intercalant in the AIBs is the much larger $AlCl_4^-$ anion. While there have been many first-principles studies investigating the diffusion mechanism of $AlCl_4^-$ anion in graphite, no conclusive agreement has been reached. The reported diffusion coefficients vary from 10^{-4} *to* 10^{-9} $cm^2\ s^{-1}$.[15–17] On the other hand, the diffusion coefficients obtained from traditional electroanalytical techniques lie between 10^{-10} and 10^{-15} $cm^2\ s^{-1}$.[18] The large variation in these values, and the discrepancies between the theory and experiments, demand a careful examination of the diffusion coefficients and the performance-limiting factors at various temperatures.

In this study, we perform diagnostic measurements of the reaction kinetics in the AIBs at several temperatures ranging from -20°C to room temperature (RT). The constant-current charge and discharge voltage curves along with the cyclic voltammogram reveal the subtle differences in the intercalation and deintercalation behavior at different temperatures. We further use the potentiostatic intermittent titration technique (PITT) and electrochemical impedance spectroscopy (EIS) to understand the fast reaction kinetics at various temperatures. Our results highlight that interfacial intercalation kinetics must be decoupled from the bulk diffusion to resolve the discrepancies in the kinetic parameters between experiments and theoretical predictions.

2. Results

2.1. Cycling at different temperatures

We performed galvanostatic cycling of the AIB pouch cells (see **Methods**) under 0.5 C current within the voltage range 1 V – 2.5 V at five different temperatures between -20°C and RT (~21°C). Unlike LIBs showing a huge capacity drop on reducing the temperature from RT to -10°C, the AIBs only had a reduction in specific discharge capacity from 96 $mAh.g^{-1}$ at RT to 82 $mAh.g^{-1}$ at -20°C, as shown in **Figure 1(a)**. The two voltage plateaus observed during both charge and discharge have been identified as stable stages of graphite, suggesting a phase separation mechanism during (de)intercalation. While the RT discharge displayed these two characteristic voltage plateaus at 1.80 V and 2.25 V, the discharge at -20°C exhibited the same plateaus at lower voltages of 1.60 V and 2.10 V. This difference is due to the fact that the reaction rate is reduced upon lowering the temperature, thus requiring a higher overpotential to overcome the activation barrier for reaction. A similar difference in the voltage plateaus was observed to occur during charging at different temperatures. Near the upper cutoff voltage, a third voltage plateau around 2.5V was observed, which in our cells did not contribute toward the discharging capacity. This irreversible plateau is attributable to potential side reactions between the electrolyte with the current collector,[19–22] as also seen in the charging voltage curves at 0°C, 10°C, and RT. The additional voltage plateau becomes more prominent as the upper cutoff voltage is slightly increased (**Figure S1**). Side reactions can reduce Coulombic efficiency at higher temperatures, as hinted in earlier reports,[7] highlighting the importance of the choice of upper cutoff voltage in the cell design. While better choices of the current collector can mitigate the side reaction and enable a reversible third intercalation plateau, the present work focuses on the fundamental intercalation and deintercalation mechanism of the $AlCl_4^-$ anion into graphite in the range of the two main voltage plateaus.

We tested the AIB pouch cells by cyclic voltammetry (CV) between 1 V and 2.5 V, with a scan rate of $1\ mV\ s^{-1}$, at five different temperatures. As the temperature increases from -20°C to RT, the positions of the respective charging peaks move forward while those during discharging move backward, consistent with the shifting of voltage plateaus we mentioned above. In addition, the absolute current density of the redox peaks in **Figure 1(b)** decreases with lowering temperatures, confirming that the reaction rate is affected by temperature.

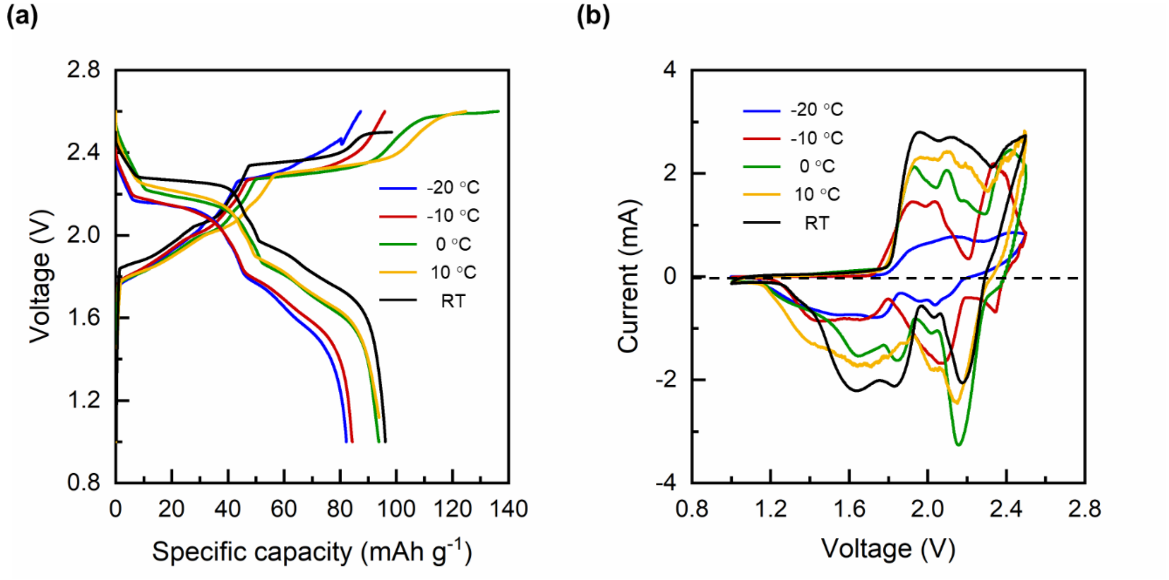

Figure 1: (a) Galvanostatic cyclic and (b) cyclic voltammetry of the AIB pouch cells. The capacity during galvanostatic discharge increased with temperature while the charging suffered from a side reaction at high voltages, leading to a ~70% Coulombic efficiency. The cyclic voltammogram showed higher peak currents at higher temperatures, confirming faster reactions at higher temperatures.

2.2. Determination of diffusion coefficients

We used the potentiostatic intermittent titration technique (PITT) between 1 V and 2.2 V during charging and between 2.5 V and 1 V during discharging, with *10 mV* potential steps at all the selected temperatures to extract the different diffusion coefficient of $AlCl_4^-$ ion into graphite cathode ($D_{AlCl_4^-}$). The threshold currents of our PITT experiments are 0.05 C for temperatures $\leqslant$ 0°C and 0.1 C for 10°C and RT. We carefully selected the aforementioned upper cutoff voltage during charging and different threshold currents at higher temperatures to avoid the side reaction observed during galvanostatic cycling. The unwanted chemical reaction, if occurring, could hamper the accurate estimation of the diffusion coefficients.

The Cottrell equation is the standard model for analyzing the transient current in response to the voltage steps in the PITT experiments, which assumes a diffusion-limited mechanism, reflected by a straight line in the Cottrell plots. However, results from our AIBs cells, like those from particulate porous electrodes for LIBs,[23,24] always show nonlinear data in the Cottrell plots, as shown in **Figures S2 – S11**, which suggest a possible mix-control mechanism. The modified PITT (mPITT) method has been successfully applied in LIBs and can provide a more comprehensive understanding of the processes,[23,25,26] via the electrochemical Biot number that relates rates between the solid-state diffusion and the surface reaction. By this definition, the "electrochemical Biot number" originally proposed by Li et al.[26,27] may be called the Damköhler number to avoid possible confusions with the classic Biot number that compares heat transfer resistance in the bulk and at the interface.

In general, the mPITT model separates the entire voltage step into two regimes: (i) short-time: $t << l^2/D_{AlCl_4^-}$ and (ii) long-time: $t >> l^2/D_{AlCl_4^-}$. We chose the transient current data within the initial 15% of the estimated diffusion time ($l^2/D_{AlCl_4^-}$) for the short-time fitting (Figures S2 – S11). Only a few voltage steps among the recorded ones generated long enough transient current to enter the long-time regime, where satisfactory fittings with the mPITT model were challenging, due to the lack of feasible *operando* characterization method to confirm the actual reacting area. According to the lithium-intercalation-induced population dynamics in similar particulate graphite,[23] the limited number of reacting particles at any time instant justify a limited reacting area much smaller than the total available interfacial area. This true reacting area is close to the apparent geometric area of the electrode.[23] We, therefore, adopted the geometric area for the data fitting.

The diffusion coefficients obtained by fitting the discharging transient currents with the mPITT model fell in the range of $10^{-9} – 10^{-7}\ cm^2\ s^{-1}$ for all cases, as shown in **Figure 2(a)-(e)**. On the other hand, the obtained Damköhler number *Da* showed a large variance at lower temperatures than higher temperatures. For instance, the B values ranged from 3 to 64 at -20°C, suggesting a transition from a diffusion-limited regime to a mixed-control regime. The B values of 1.14 – 2.25 for the RT case indicate the mixed-control mechanism. This result further confirmed that directly using the Cottrell equation to extract the diffusion coefficient based on the diffusion-limited assumption is not strictly valid, although practically an approximation of the curved data with a straight Cottrell line may yield similar diffusion coefficients (Figure 2). The physical insights provided by the Damköhler number, however, are necessary, as they are critical for determining whether modifying the particle size or morphology will enable better (de)intercalation dynamics. The average value of $D_{AlCl_4^-}$ increased with increasing temperature, as shown in **Figure 2(f)**.

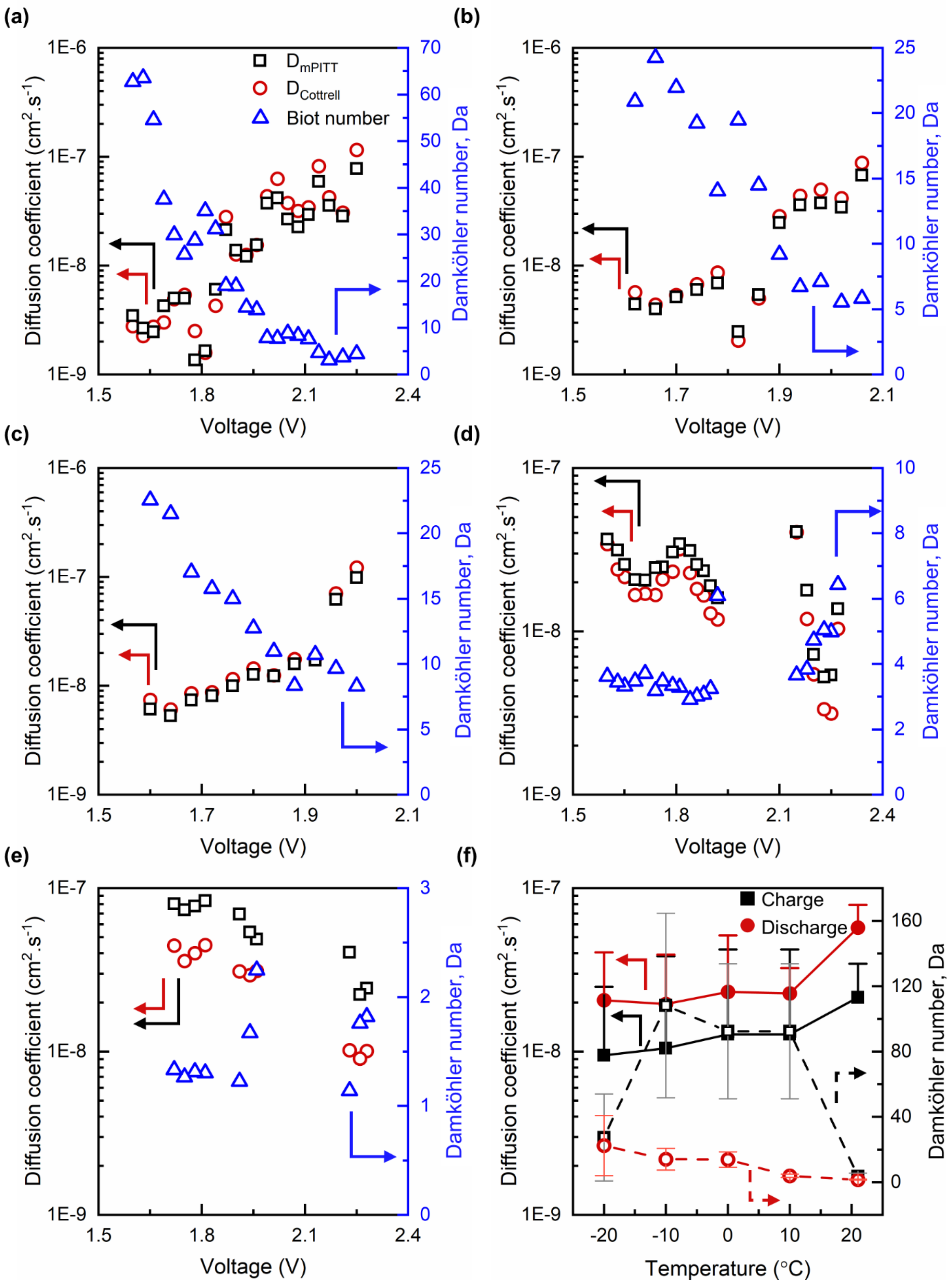
(a)
1E-6
1E-7
1E-8
1E-9
Diffusion coefficient (cm^2.s^{-1})
D_{mPITT}
$D_{Cottrell}$
Biot number
70
60
50
40
30
20
10
0
Damköhler number, Da
1.5
1.8
2.1
2.4
Voltage (V)
(b)
1E-6
1E-7
1E-8
1E-9
Diffusion coefficient (cm^2.s^{-1})
25
20
15
10
5
0
Damköhler number, Da
1.5
1.7
1.9
2.1
Voltage (V)
(c)
1E-6
1E-7
1E-8
1E-9
Diffusion coefficient (cm^2.s^{-1})
25
20
15
10
5
0
Damköhler number, Da
1.5
1.7
1.9
2.1
Voltage (V)
(d)
1E-7
1E-8
1E-9
Diffusion coefficient (cm^2.s^{-1})
10
8
6
4
2
0
Damköhler number, Da
1.5
1.8
2.1
2.4
Voltage (V)
(e)
1E-7
1E-8
1E-9
Diffusion coefficient (cm^2.s^{-1})
3
2
1
0
Damköhler number, Da
1.5
1.8
2.1
2.4
Voltage (V)
(f)
1E-7
1E-8
1E-9
Diffusion coefficient (cm^2.s^{-1})
Charge
Discharge
160
120
80
40
0
Damköhler number, Da
-20
-10
0
10
20
Temperature (°C)

Figure 2: Potentiostatic titration intermittent technique (PITT) at different temperatures. The solid-state diffusion coefficients (black rectangle) and Damköhler number (blue triangle) are obtained during discharging from the mPITT method at (a) -20°C, (b) -10°C, (c) 0°C, (d) 10°C, and (e) RT. The panels (a)-(e) also show the diffusion coefficients obtained using the Cottrell equation for comparison. (f) Average diffusion coefficients and Damköhler numbers during charge and discharge. The average diffusion coefficients increase with temperature during both charge and discharge. The Damköhler numbers indicate that the process is diffusion-limited at -20°C but becomes mixed-control at RT. The thicker and darker error bars represent the standard deviations in the diffusion coefficients at each temperature. Since the left Y-axis is logarithmic scale, the minus error bars appear much longer than the plus error bars. Thus, only plus error bar is plotted. The lighter and thinner error bars are the standard deviations of the Damköhler numbers at each temperature.

2.3. Temperature-insensitive Kinetics Revealed by Impedance Analysis

While the mPITT model is self-sufficient for the evaluation of the exchange current density j_0 via the expression $B = -j_0(\partial U/\partial C)/(D_{AlCl_4^-}RT)$, where $\partial U/\partial C$ is the derivative of the open-circuit voltage with respect to the anion concentration in the solid-state, R is the gas constant and T is the temperature,[26] its evaluation for the ideal phase transformation materials is impossible due to $\partial U/\partial C$ being zero. Hence, we performed electrochemical impedance spectroscopy (EIS) for an independent evaluation of j_0. We obtained the impedance spectra of the AIBs at several state-of-charges (SOCs) between 0% and 100% during both charging and discharging at all the five selected temperatures, with 0% SOC indicating empty graphite while 100% SOC indicating the highest intercalated state. **Figure S22** shows the fitting of all the impedance spectra along with the fitting values in **Section 6.2** of the Supplementary Information. We charge or discharge the battery at a current of 0.5 C to the desired SOC and provide relaxation of 2 hours to achieve equilibrium before running an EIS. The Nyquist plots exhibited two semicircles followed by a straight line, modeled by the equivalent circuit displayed in **Figure 3(a)-(b)**. Here, the Warburg tail represents the solid-state diffusion in the graphite particles,[28] and the charge-transfer resistance can be calculated by measuring the diameter of the second semicircle. Generally, charge-transfer resistance governs the reaction kinetics, and its higher value represents a sluggish reaction. The initial charge-transfer resistance at -20°C was 7-folds higher than RT but was less than 4.4 times the RT charge transfer resistance at other SOCs. Moreover, the charge-transfer resistance only reaches a maximum of twice the RT value for higher temperatures as shown in Figure 3(a)-(b). This trend is in contrast with the LIBs where the charge-transfer resistance increases drastically and becomes nearly 15 times of the RT at -10°C. Such a drastic increase slows the reaction rate in LIBs at low temperatures causing poor performance. In the case of AIBs, since the increase in charge-transfer resistance is not as severe as LIBs, they can provide a substantial capacity at lower temperatures, demonstrating their potential viability for low-temperature climates.

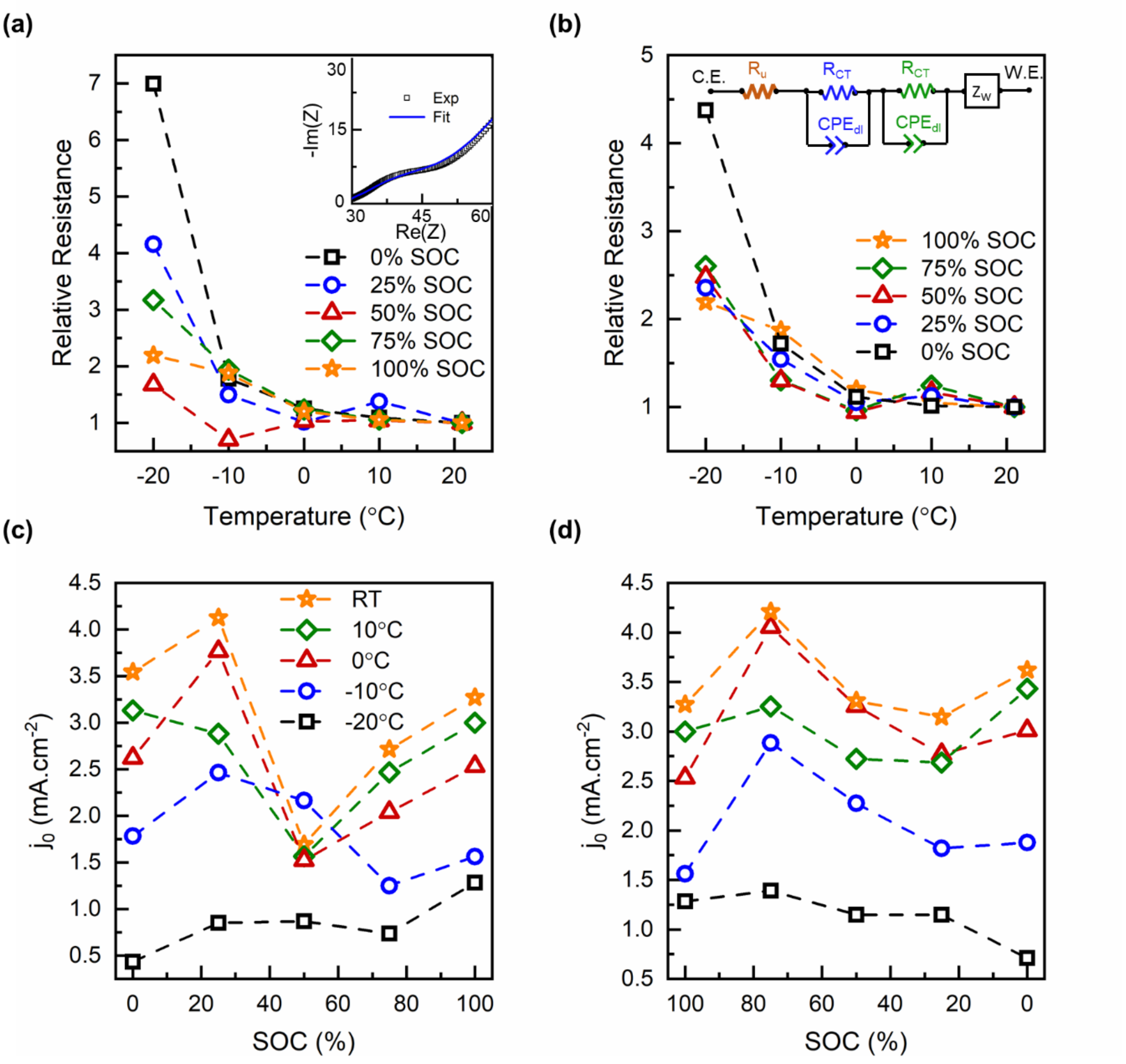

Figure 3: Temperature-dependent properties of AIBs revealed by impedance analysis. Charge-transfer resistance relative to the RT at the five temperatures at the selected SOCs during (a) charge, and (b) discharge. Inset in panel (a) shows a typical Nyquist plot showing two semicircles followed by a Warburg tail. Panel (b) also shows the equivalent circuit used to fit all the Nyquist plots. Exchange current density obtained from the charge-transfer resistances at the five temperatures during (c) charge, and (d) discharge. The charge-transfer resistances reduce with increasing temperature, leading to faster reactions but the decay is much smaller as compared to the LIBs. The fastest reaction at RT results in the highest exchange current densities. The hysteresis in the exchange current densities arises due to an assumption of the constant active area in the estimation.

Exchange current density is a material property that characterizes the surface reaction at the electrode-electrolyte interface, often calculated using the Butler-Volmer equation.[29] At low overpotentials, the Butler-Volmer equation for j_0 simplifies to $j_0 = RT/(FAR_{CT})$, where R_{CT} is the charge-transfer resistance and A is the active area for reaction, assumed as the geometric area for simplification.[25] As shown in **Figure 3(c)-(d)**, our experiments confirmed that the j_0 for the surface reaction was between 0.5 and $1.4\ mA\ cm^{-2}$ at -20°C and as high as $4.2\ mA\ cm^{-2}$ at RT. In addition to the temperature dependence, the exchange current density for our system was highly SOC-dependent, as is the case for many other electrochemical systems.[29,30] Comparing Figure 3(c) and 3(d) reveals the existence of a slight hysteresis in j_0 between charge and discharge. Charging-discharging hysteresis has been observed in many battery cathode materials, including $LiFePO_4$, NMC, and NCA in LIBs, potentially attributable to phase transformation,[31] or crack formation,[25] both of which would affect the actual reacting area, hence affect the overpotential. As shown in a recent study for the graphite electrodes for lithium intercalation, the actual reacting area of the porous electrode is highly dependent on both the applied current and the exchange current density.[24] In the present study, we exploit our experience with lithium intercalation in graphite and extracted the SOC-dependent j_0 for anion intercalation in graphite at various temperatures for the first time.

2.4. Ionic Species in the Electrical double layer structure

The surprisingly fast low-temperature kinetics of graphite in AIBs may be explained by the temperature-insensitive supply of active species within the electrical double layer (EDL) structure, due to the lack of inactive but indispensable polar solvent molecules, e.g., ethylene carbonate (EC) that stabilizes carbonaceous anodes for LIBs, that may crowd into the inner Helmholtz layer. Here in AIBs, the ionic liquid consists of two salts without any solvent molecules, allowing a high concentration of active species without a blocking layer of inactive solvent molecules at the electrode surface to impede the charge transfer reaction.[32] The EDL structure was simulated via classical molecular dynamics (cMD) by applying surface charges to a Cu current collector as a proxy for the graphite electrode surface during operation.[33] As the surface charge is set to ±0.1 $C.m^{-2}$ at RT, the aluminum anode as represented by the negatively charged Cu was crowded by the parallelly-oriented $[EMIm]^+$ ions in the inner Helmholtz plane of the EDL to screen the surface charge, followed by a layer of the $AlCl_4^-$ ions to maintain the local neutrality (**Figure 4 (a)**). At the cathode side with a positive surface charge, we see a much lower concentration of the $[EMIm]^+$ ions near the electrode surface, and the $AlCl_4^-$ anions can easily reach the electrode surface to complete the fast reaction. Moreover, most of the $[EMIm]^+$ ions arrange perpendicular to the surface owing to their partial charges as shown in **Figure S24**.[34] Based on the averaged concentration from the last 2 ns of the simulation, the EDL structure shows alternating layers of cations (**Figure 4 (b)**), with little influence from the low temperature. Our MD simulations at -20°C, shown in **Figure S23**, showed similarity in the distribution of ions in the electric double layers at both the electrodes, compared to RT. We observed almost no change in the average ion concentrations in the double layers when the temperature dropped from RT to -20°C. The enriched but oscillating concentrations of active species damp to their bulk concentrations at around 20 Å. Moreover, the bulky anions with a diameter of 10.70 Å are in close contact with the cathode surface, as indicated by the length of horizontal error bars in Figure 4(b). Increasing the surface charge linearly decreases the concentration of $[EMIm]^+$ in the EDL while that of $AlCl_4^-$ remains relatively constant and fluctuates between 1.0 – 3.5 M (**Figure 4 (c)**). Such temperature-insensitive distributions support the easy accessibility of the $AlCl_4^-$ anions for fast intercalation at the graphite surface, even at low temperatures such as -20°C, yielding a smaller difference in the charge-transfer resistances between -20°C and RT.

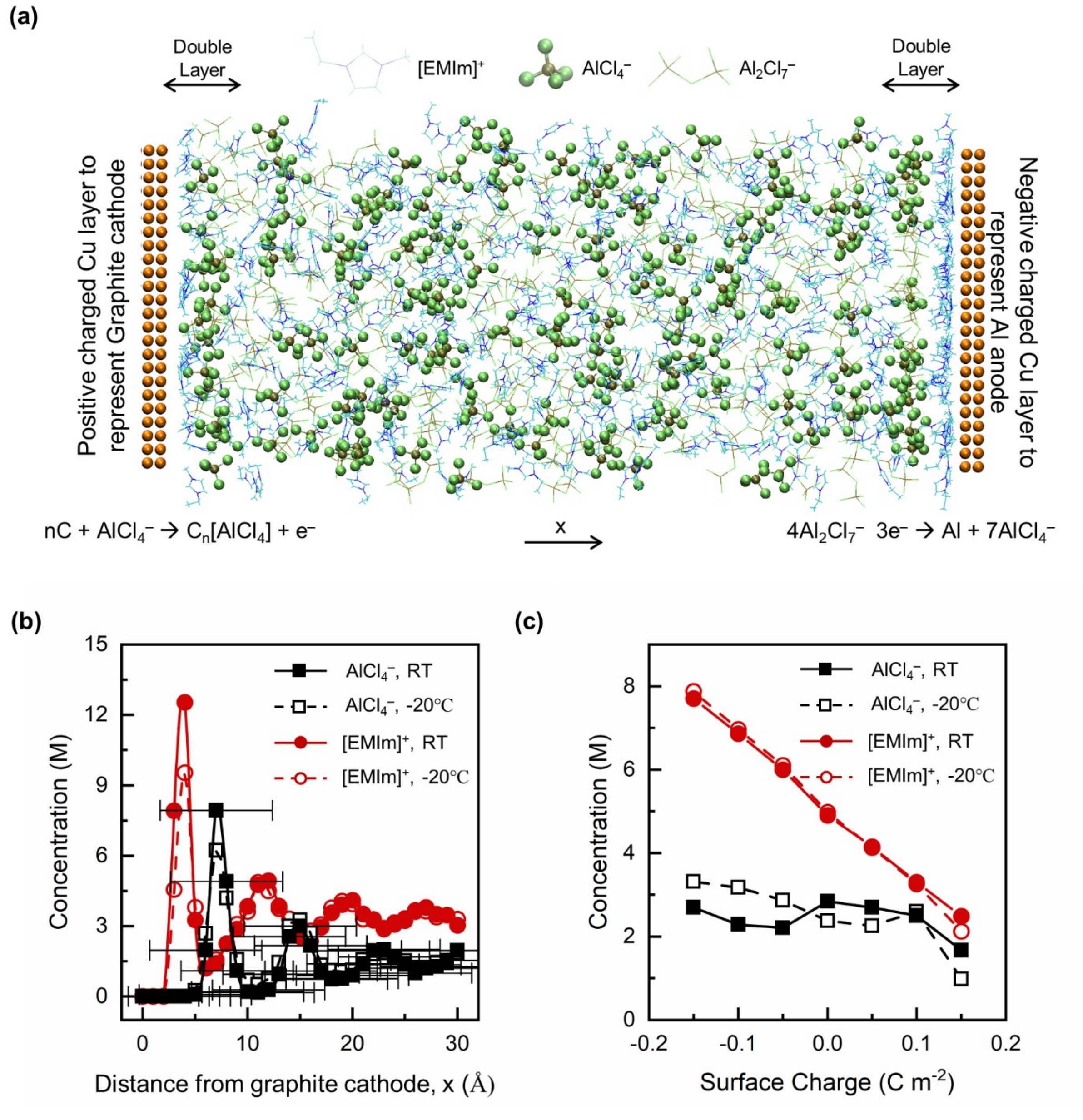

Figure 4: Molecular Dynamics simulation of AIB at RT and -20°C. (a) Structure of the electric double layer near the cathode and anode with the surface charge of ±0.1 C m^{-2}, along with the bulk at RT obtained from MD simulation. The electrodes are represented by positive and negative charged Cu layers. The MD simulation shows a high concentration of $AlCl_4^-$ anions at the cathode at RT. (b) Absolute concentrations of $[EMIm]^+$ and $AlCl_4^-$ ions within 30 Å from the graphite cathode with surface charge 0.1 C m^{-2}. The profile

is obtained from averaging the final 2 ns of the simulation. The horizontal error bars on the concentration of $AlCl_4^-$ ions indicate their diameter, suggesting that they are already close to the charged electrode surface. (c) Average concentrations of $[EMIm]^+$ and $AlCl_4^-$ ions in the double layer at surface charges 0, ± 0.05, ± 0.1, and ± 0.15 C m^{-2}, at RT and -20°C temperatures.

3. Discussion

The galvanostatic cycling, along with CV, PITT, and EIS, provided valuable insights into the reaction kinetics governing the anion intercalation and deintercalation into the graphite cathodes in AIBs. In addition to the higher activation barrier for the surface reaction at low temperatures, the increased (decreased) operating voltage during galvanostatic charge (discharge) has been ascribed to a rise in electric polarization caused by decreased ionic conductivities of both the electrolyte and the SEI.[5] This effect appears less severe in AIBs than in LIBs, owing to the smaller drop in the ionic conductivity of the ionic liquid[35] from *15* $mS.cm^{-1}$ at RT to *9* $mS.cm^{-1}$ at -20°C, in stark contrast to the reported drop in LIB from *9* $mS.cm^{-1}$ at RT to *3* $mS.cm^{-1}$ at -20°C.[5] Although the increased overpotentials at lower temperatures would reduce the total capacities, the galvanostatic cycling and CV alone did not allow the rigorous investigation of the fundamental governing mechanisms. Combined with the independent EIS, the mPITT method provided a more detailed understanding of the reaction mechanisms in the AIBs. Our modeling suggested that both the diffusion (derived from $D_{AlCl_4^-}$) and surface reaction (derived from j_0) slowed down with decreasing temperature from RT to -20°C. However, the charge transfer mechanism shifted from mixed control at RT to diffusion control at -20°C. Assuming diffusion limitation from the Cottrell method, reducing the particle size would enhance the diffusion and the overall charge transfer. But, according to the insights from mPITT fitting, smaller particles would help the charge transfer at low temperatures to overcome the diffusion limitation, while higher surface area would enable faster surface reaction and avoid reaction limitation at higher temperatures. Thus, a robust electrode design for AIB would require an optimal particle size and surface morphology for better performance to operate under a relatively wide range of weather conditions.

The study confirms a mild increase in the charge-transfer resistance with decreasing temperature in AIBs, owing to the high availability of active species in the electric double layer even at low temperatures. In addition to the structures and local concentrations obtained from MD simulations, explicitly including the EDL contribution in the Butler-Volmer equation, e.g., via a modified Frumkin-Butler-Volmer equation[36], may further improve the mPITT method. Adopting the microscopic Marcus theory[37,38] and connecting the desolvation energy of active species at the inner Helmholtz plane with the reorganization energy[39,40] may provide quantitative explanations of the charge transfer resistance and the exchange current density, without using free fitting parameters. Since the ionic liquids exhibit different EDL structures than the polar solvent electrolytes,[32,41] the inclusion of EDL effects in the reaction kinetics especially becomes necessary for ionic liquids.

The understanding of the rate-governing mechanisms in the particulate phase-transforming electrodes is a multi-faceted multi-scale problem. While in the present study, we investigated the two important kinetic parameters, and their competing characteristics at various conditions, the anion-intercalation-induced phase-transformation dynamics at the single-particle level and the porous electrode level are important. Single-particle observations will aid in a deeper examination of the fundamental solid-state nucleation process. Mesoscale *operando* experiments at the electrode level will also be beneficial for a complete diagnosis of the population dynamics to facilitate the electrode design, as performed recently for LIBs.[23,24] The combined understanding coupled with a consistent thermodynamic model would be essential in determining the phase transformation mechanisms, crucial for the long-term performance of the AIBs.

4. Conclusion

We have performed a systematic electrochemical characterization, at five different temperatures, to assess the high-rate bulky anion intercalation in graphite electrodes of the AIBs invented by Dai et al.[12,42,43]. We adopted the modified PITT (mPITT) method and EIS to estimate the kinetic parameters and gauge the rate-limiting steps. Without the assumption of the diffusion limitation as in the Cottrell method, self-consistent diffusion coefficients ($10^{-9} - 10^{-7}$ cm^2 s^{-1}) and the exchange current densities ($0.5 - 4.2$ mA cm^{-2}) were obtained, both of which increase with increasing temperature, but the governing process changes from mixed control at RT to diffusion control at -20°C, as revealed by the Damköhler number. In stark contrast to LIBs that suffer from a 40-times increase of charge transfer resistance[5] upon decreasing the temperature from on reducing the temperature from RT to -20°C, the charge transfer resistance for the intercalation of much bulkier anion into similar graphite electrodes only increases up to five times. Our analysis suggested that the synergy of fast diffusion, low interfacial resistance, and high availability of the active species in the double layer enabled the surprising high-rate performance at low temperatures. Future research of incorporating explicitly the dielectric and concentration characteristics of the electrical double layer structure into charge transfer kinetics may enable more accurate quantitative understandings of the interfacial processes and help translate the insight from AIBs to low-temperature LIBs.

5. Methods

Preparation of graphite electrode: We formed a homogeneous graphite slurry by dispersing SP-1 graphite powder (TED PELLA, Inc.) and PVdF binder (>99.5%, MTI Corp) in the ratio 90:10, in 1-methyl-2-pyrrolidone (NMP, 99.5%, Sigma Aldrich). This slurry was coated onto Cu foil by the doctor-blade method. We, then, dried the electrodes at 60°C to remove the NMP and punched out Φ8 mm electrodes. The Cu foil was then etched by immersing the punched electrodes into 2.5M iron chloride (Sigma Aldrich, 97%) solution to form free-standing graphite film. Finally, these graphite films were rinsed with deionized water to remove the residual $FeCl_3$ and dried at 70°C for 12 hours to obtain the graphite electrode for AIB.

Preparation of ionic liquid electrolyte: We formed the ionic liquid electrolyte for AIB by mixing 1-Ethyl-3-methylimidazolium chloride ([EMIm]Cl) (Sigma Aldrich, 98%) and anhydrous $AlCl_3$ (Alfa Aesar, 99%). [EMIm]Cl was dried at 70°C under vacuum for 24 hours to remove residual water. The ionic liquid was prepared by mixing $AlCl_3$ with dried [EMIm]Cl in the molar ratio 1.7:1 in an Ar-filled glove box. After stirring for 15 minutes, we obtained a light-yellow, transparent liquid.

Fabrication of pouch cell: We assembled pouch cells in the Ar-filled glovebox using the free-standing graphite cathode and an Al foil anode, separated by al layer of glass fiber separator. We used polymer-coated Ni tabs as current collectors and attached them to both the electrodes using carbon tape (TED PELLA, Inc.). We used the ionic liquid as electrolyte and sealed the pouch cell using a heat sealer. After removing the cell from the glovebox, we held it between two glass slides supported by a binder clip. The cell assembly was connected to the LAND battery tester for electrochemical experiments.

mPITT method: Adopting the method developed by Li et al.[26], the analytical solution of $AlCl_4^-$ ion diffusion in graphite particles is

$$\frac{C(x,t)-C_0}{C_S-C_0} = 1 - 2Da\sum_{n=1}^{\infty}\frac{\cos\left[\lambda_n\left(1-\frac{x}{l}\right)\right]}{(\lambda_n^2+Da^2+Da)\cos\lambda_n}\exp\left(-\lambda_n^2\frac{D_{AlCl_4^-}t}{l^2}\right)$$

where $Da = -\frac{l(j_0|_S)(\partial U/\partial C|_S)}{D_{AlCl_4^-}RT}$ is the dimensionless Damköhler number, a ratio of the diffusion resistance and the resistance due to surface reaction. λ_1 is the 1st positive root of equation $\lambda_1 \tan\lambda_1 = Da$. For our systems, the term $(C_S - C_0)$ can be replaced with the total charge transferred in the applied potential step using Faraday's law as $Q_T = zFSl(C_S - C_0)$, where S is the geometric area of the electrode and l is the diffusion length. Neglecting higher order terms, the transient current can be written as Equation (1) for $t << l^2/D_{Li}$ and as Equation (2) for $t >> l^2/D_{Li}$

$$I(t) = \frac{D_{AlCl_4^-}Q}{l^2}Da\exp\left(Da^2\frac{D_{AlCl_4^-}t}{l^2}\right)erfc\left(Da\sqrt{\frac{D_{AlCl_4^-}t}{l^2}}\right) \tag{1}$$

$$\ln[I(t)] = -\lambda_1^2\left(\frac{D_{AlCl_4^-}t}{l^2}\right) + \ln\left[\frac{2QD_{AlCl_4^-}}{l^2}\frac{Da^2}{(\lambda_1^2+Da^2+Da)}\right] \tag{2}$$

Both Da and $D_{AlCl_4^-}$ were estimated by fitting the experimental transient currents with the above analytical expressions by minimizing least squares using MATLAB.

MD simulation: The classical MD simulation was performed at constant volume and temperature (NVT) to the electrolyte-electrode nano-slit geometry[33] with two 40×40×20 Å^3 Cu electrodes in an FCC lattice sandwiching the 40×40×100 Å^3 electrolyte. According to the corresponding product stoichiometry of $AlCl_3$:[EMIm]Cl as 1.7:1,[44] the simulation box contains 351 $[EMIm]^+$, 140 $AlCl_4^-$, and 176 $Al_2Cl_7^-$. The model was constructed using the all-atom force field developed by Lopes et al.[45] for imidazolium cation and parameters developed by Mains et al. for anions[46] with geometric combination rules for the Lennard-Jones parameters between different atom types. Surface charge was applied by placing partial charge on the first layer of Cu atoms. Equilibration was performed at 1 fs time step for 10 ns without surface charge, followed by 20 ns simulation for each surface charge ramping continuously from ±0.05 to ±0.15 C.m^2. The final 2 ns of each surface charge was used for data collection. The initial configuration was generated by the open-source software Moltemplate and PACKMOL.[47,48] RDF analysis and visualization were performed using VMD.[49]

Acknowledgment

P.B. acknowledges the support from a National Science Foundation grant (Award No. 2044932) and the faculty startup support from Washington University in St. Louis. The materials characterization experiments were partially supported by IMSE (Institute of Materials Science and Engineering) and by a grant from InCEES (International Center for Energy, Environment and Sustainability) at Washington University in Saint Louis. The authors thank Dr. Michael McEldrew for his helpful comments.

Author contributions

P.B. conceived and supervised the study. S.A. and P.B. designed the experiments. S.A., J.W. and R.S. performed the experiments. B.M. performed the MD simulations. S.A., N.M. and B.M. carried out the analysis. S.A and P.B. wrote and revised the manuscript.

Additional information

Supplementary information is available online.

Competing interests

The authors declare no competing financial interests.

Data availability

The data that support the findings of this study are available from the corresponding author upon reasonable request.

Code availability

The MATLAB codes for mPITT fitting are available from the corresponding author upon reasonable request.

References

(1) Tarascon, J. M.; Armand, M. Issues and Challenges Facing Rechargeable Lithium Batteries. *Nature* **2001**, *414* (6861), 359–367. https://doi.org/10.1038/35104644.

(2) Choi, J. W.; Aurbach, D. Promise and Reality of Post-Lithium-Ion Batteries with High Energy Densities. *Nat. Rev. Mater.* **2016**, *1*. https://doi.org/10.1038/natrevmats.2016.13.

(3) Goodenough, J. B.; Kim, Y. Challenges for Rechargeable Li Batteries. *Chem. Mater.* **2010**, *22* (3), 587–603. https://doi.org/10.1021/cm901452z.

(4) Petzl, M.; Kasper, M.; Danzer, M. A. Lithium Plating in a Commercial Lithium-Ion Battery - A Low-Temperature Aging Study. *J. Power Sources* **2015**, *275*, 799–807. https://doi.org/10.1016/j.jpowsour.2014.11.065.

(5) Zhang, S. S.; Xu, K.; Jow, T. R. The Low Temperature Performance of Li-Ion Batteries. *J. Power Sources* **2003**, *115* (1), 137–140. https://doi.org/10.1016/S0378-7753(02)00618-3.

(6) Zhu, G.; Wen, K.; Lv, W.; Zhou, X.; Liang, Y.; Yang, F.; Chen, Z.; Zou, M.; Li, J.; Zhang, Y.; He, W. Materials Insights into Low-Temperature Performances of Lithium-Ion Batteries. *J. Power Sources* **2015**, *300*, 29–40. https://doi.org/10.1016/j.jpowsour.2015.09.056.

(7) Pan, C. J.; Yuan, C.; Zhu, G.; Zhang, Q.; Huang, C. J.; Lin, M. C.; Angell, M.; Hwang, B. J.;

Kaghazchi, P.; Dai, H. An Operando X-Ray Diffraction Study of Chloroaluminate Anion-Graphite Intercalation in Aluminum Batteries. *Proc. Natl. Acad. Sci. U. S. A.* **2018**, *115* (22), 5670–5675. https://doi.org/10.1073/pnas.1803576115.

(8) Zhang, Y.; Liu, S.; Ji, Y.; Ma, J.; Yu, H. Emerging Nonaqueous Aluminum-Ion Batteries: Challenges, Status, and Perspectives. *Adv. Mater.* **2018**, *30* (38). https://doi.org/10.1002/adma.201706310.

(9) Elia, G. A.; Marquardt, K.; Hoeppner, K.; Fantini, S.; Lin, R.; Knipping, E.; Peters, W.; Drillet, J. F.; Passerini, S.; Hahn, R. An Overview and Future Perspectives of Aluminum Batteries. *Adv. Mater.* **2016**, *28* (35), 7564–7579. https://doi.org/10.1002/adma.201601357.

(10) Ambroz, F.; Macdonald, T. J.; Nann, T. Trends in Aluminium-Based Intercalation Batteries. *Adv. Energy Mater.* **2017**, *7* (15). https://doi.org/10.1002/aenm.201602093.

(11) Das, S. K.; Mahapatra, S.; Lahan, H. Aluminium-Ion Batteries: Developments and Challenges. *J. Mater. Chem. A* **2017**, *5* (14), 6347–6367. https://doi.org/10.1039/c7ta00228a.

(12) Wang, D. Y.; Wei, C. Y.; Lin, M. C.; Pan, C. J.; Chou, H. L.; Chen, H. A.; Gong, M.; Wu, Y.; Yuan, C.; Angell, M.; Hsieh, Y. J.; Chen, Y. H.; Wen, C. Y.; Chen, C. W.; Hwang, B. J.; Chen, C. C.; Dai, H. Advanced Rechargeable Aluminium Ion Battery with a High-Quality Natural Graphite Cathode. *Nat. Commun.* **2017**, *8*, 1–7. https://doi.org/10.1038/ncomms14283.

(13) Wei, J.; Chen, W.; Chen, D.; Yang, K. An Amorphous Carbon-Graphite Composite Cathode for Long Cycle Life Rechargeable Aluminum Ion Batteries. *J. Mater. Sci. Technol.* **2018**, *34* (6), 983–989. https://doi.org/10.1016/j.jmst.2017.06.012.

(14) Wang, S.; Yu, Z.; Tu, J.; Wang, J.; Tian, D.; Liu, Y.; Jiao, S. A Novel Aluminum-Ion Battery: Al/AlCl3-[EMIm]Cl/Ni3S2@Graphene. *Adv. Energy Mater.* **2016**, *6* (13), 2–11. https://doi.org/10.1002/aenm.201600137.

(15) Gao, Y.; Zhu, C.; Chen, Z. Z.; Lu, G. Understanding Ultrafast Rechargeable Aluminum-Ion Battery from First-Principles. *J. Phys. Chem. C* **2017**, *121* (13), 7131–7138. https://doi.org/10.1021/acs.jpcc.7b00888.

(16) Wu, M. S.; Xu, B.; Chen, L. Q.; Ouyang, C. Y. Geometry and Fast Diffusion of AlCl4 Cluster Intercalated in Graphite. *Electrochim. Acta* **2016**, *195*, 158–165. https://doi.org/10.1016/j.electacta.2016.02.144.

(17) Jung, S. C.; Kang, Y. J.; Yoo, D. J.; Choi, J. W.; Han, Y. K. Flexible Few-Layered Graphene for the Ultrafast Rechargeable Aluminum-Ion Battery. *J. Phys. Chem. C* **2016**, *120* (25), 13384–13389. https://doi.org/10.1021/acs.jpcc.6b03657.

(18) Hu, H.; Cai, T.; Bai, P.; Xu, J.; Ge, S.; Hu, H.; Wu, M.; Xue, Q.; Yan, Z.; Gao, X.; Xing, W. Small Graphite Nanoflakes as an Advanced Cathode Material for Aluminum Ion Batteries. *Chem. Commun.* **2020**, *56* (10), 1593–1596. https://doi.org/10.1039/c9cc06895c.

(19) Reed, L. D.; Menke, E. The Roles of V 2 O 5 and Stainless Steel in Rechargeable Al–Ion Batteries . *J. Electrochem. Soc.* **2013**, *160* (6), A915–A917. https://doi.org/10.1149/2.114306jes.

(20) Chiku, M.; Takeda, H.; Matsumura, S.; Higuchi, E.; Inoue, H. Amorphous Vanadium Oxide/Carbon Composite Positive Electrode for Rechargeable Aluminum Battery. *ACS Appl. Mater. Interfaces* **2015**, *7* (44), 24385–24389. https://doi.org/10.1021/acsami.5b06420.

(21) Nakayama, Y.; Senda, Y.; Kawasaki, H.; Koshitani, N.; Hosoi, S.; Kudo, Y.; Morioka, H.; Nagamine, M. Sulfone-Based Electrolytes for Aluminium Rechargeable Batteries. *Phys. Chem. Chem. Phys.* **2015**, *17* (8), 5758–5766. https://doi.org/10.1039/c4cp02183e.

(22) Wang, S.; Jiao, S.; Song, W. L.; Chen, H. Sen; Tu, J.; Tian, D.; Jiao, H.; Fu, C.; Fang, D. N. A Novel Dual-Graphite Aluminum-Ion Battery. *Energy Storage Mater.* **2018**, *12* (December 2017), 119–127. https://doi.org/10.1016/j.ensm.2017.12.010.

(23) Agrawal, S.; Bai, P. Operando Electrochemical Kinetics in Particulate Porous Electrodes by Quantifying the Mesoscale Spatiotemporal Heterogeneities. *Adv. Energy Mater.* **2021**, *203344*, 1–12. https://doi.org/10.1002/aenm.202003344.

(24) Agrawal, S.; Bai, P. Interplay between Phase Transformation Instabilities and Spatiotemporal Reaction Heterogeneities in Particulate Intercalation Electrodes. *arXiv* **2021**, *2110.13403*.

(25) Tsai, P. C.; Wen, B.; Wolfman, M.; Choe, M. J.; Pan, M. S.; Su, L.; Thornton, K.; Cabana, J.; Chiang, Y. M. Single-Particle Measurements of Electrochemical Kinetics in NMC and NCA Cathodes for Li-Ion Batteries. *Energy Environ. Sci.* **2018**, *11* (4), 860–871. https://doi.org/10.1039/c8ee00001h.

(26) Li, J.; Xiao, X.; Yang, F.; Verbrugge, M. W.; Cheng, Y. T. Potentiostatic Intermittent Titration Technique for Electrodes Governed by Diffusion and Interfacial Reaction. *J. Phys. Chem. C* **2012**, *116* (1), 1472–1478. https://doi.org/10.1021/jp207919q.

(27) Li, J.; Yang, F.; Xiao, X.; Verbrugge, M. W.; Cheng, Y. T. Potentiostatic Intermittent Titration Technique (PITT) for Spherical Particles with Finite Interfacial Kinetics. *Electrochim. Acta* **2012**, *75*, 56–61. https://doi.org/10.1016/j.electacta.2012.04.050.

(28) Ho, C.; Raistrick, I. D.; Huggins, R. A. Application of A-C Techniques to the Study of Lithium Diffusion in Tungsten Trioxide Thin Films. *J. Electrochem. Soc.* **1980**, *127* (2), 343–350. https://doi.org/10.1149/1.2129668.

(29) Newman, J.; Thomas-alyea, K. E. *Electrochemical Systems*; John Wiley & Sons, Inc., New York, NY: Berkeley, 2004.

(30) Doyle, M.; Fuller, T. F.; Newman, J. Modeling of Galvanostatic Charge and Discharge of the Lithium/Polymer/Insertion Cell. *J. Electrochem. Soc.* **1993**, *140* (6), 1526–1533. https://doi.org/10.1149/1.2221597.

(31) Dreyer, W.; Jamnik, J.; Guhlke, C.; Huth, R.; Moškon, J.; Gaberšček, M. The Thermodynamic Origin of Hysteresis in Insertion Batteries. *Nat. Mater.* **2010**, *9* (5), 448–453. https://doi.org/10.1038/nmat2730.

(32) Oldham, K. B. A Gouy-Chapman-Stern Model of the Double Layer at a (Metal)/(Ionic Liquid) Interface. *J. Electroanal. Chem.* **2008**, *613* (2), 131–138. https://doi.org/10.1016/j.jelechem.2007.10.017.

(33) McEldrew, M.; Goodwin, Z. A. H.; Kornyshev, A. A.; Bazant, M. Z. Theory of the Double Layer in Water-in-Salt Electrolytes. *J. Phys. Chem. Lett.* **2018**, *9* (19), 5840–5846. https://doi.org/10.1021/acs.jpclett.8b02543.

(34) Frolov, A. I.; Kirchner, K.; Kirchner, T.; Fedorov, M. V. Molecular-Scale Insights into the Mechanisms of Ionic Liquids Interactions with Carbon Nanotubes. *Faraday Discuss.* **2012**, *154*, 235–247. https://doi.org/10.1039/c1fd00080b.

(35) Cosby, T.; Durkin, D. P.; Mantz, R. A.; Trulove, P. C. Ion Dynamics and Charge Transport in Imidazolium Chloroaluminate Ionic Liquids. *ECS Meet. Abstr.* **2021**, *MA2021-01* (7), 424–424. https://doi.org/10.1149/ma2021-017424mtgabs.

(36) Biesheuvel, P. M.; van Soestbergen, M.; Bazant, M. Z. Imposed Currents in Galvanic Cells. *Electrochim. Acta* **2009**, *54* (21), 4857–4871. https://doi.org/10.1016/j.electacta.2009.03.073.

(37) Marcus, R. A. Electrostatic Free Energy and Other Properties of States Having Nonequilibrium Polarization. I. *J. Chem. Phys.* **1956**, *24* (5), 979–989. https://doi.org/10.1063/1.1742724.

(38) Bai, P.; Bazant, M. Z. Charge Transfer Kinetics at the Solid-Solid Interface in Porous Electrodes. *Nat. Commun.* **2014**, *5*, 1–7. https://doi.org/10.1038/ncomms4585.

(39) Bangle, R. E.; Schneider, J.; Piechota, E. J.; Troian-Gautier, L.; Meyer, G. J. Electron Transfer Reorganization Energies in the Electrode-Electrolyte Double Layer. *J. Am. Chem. Soc.* **2020**, *142*

(2), 674–679. https://doi.org/10.1021/jacs.9b11815.

(40) Xiao, T.; Song, X. Reorganization Energy of Electron Transfer Processes in Ionic Fluids: A Molecular Debye-Hückel Approach. *J. Chem. Phys.* **2013**, *138* (11). https://doi.org/10.1063/1.4794790.

(41) Kornyshev, A. A. Double-Layer in Ionic Liquids: Paradigm Change? *J. Phys. Chem. B* **2007**, *111* (20), 5545–5557. https://doi.org/10.1021/jp067857o.

(42) Lin, M. C.; Gong, M.; Lu, B.; Wu, Y.; Wang, D. Y.; Guan, M.; Angell, M.; Chen, C.; Yang, J.; Hwang, B. J.; Dai, H. An Ultrafast Rechargeable Aluminium-Ion Battery. *Nature* **2015**, *520* (7547), 325–328. https://doi.org/10.1038/nature14340.

(43) Pan, C. J.; Yuan, C.; Zhu, G.; Zhang, Q.; Huang, C. J.; Lin, M. C.; Angell, M.; Hwang, B. J.; Kaghazchi, P.; Dai, H. An Operando X-Ray Diffraction Study of Chloroaluminate Anion-Graphite Intercalation in Aluminum Batteries. *Proc. Natl. Acad. Sci. U. S. A.* **2018**, *115* (22), 5670–5675. https://doi.org/10.1073/pnas.1803576115.

(44) Shinde, P.; Ahmed, A. N.; Nahian, M. K.; Peng, Y.; Reddy, R. G. Conductivity of 1-Ethyl-3-Methylimidazolium Chloride (EMIC) and Aluminum Chloride (AlCl 3) Ionic Liquids at Different Temperatures and AlCl 3 Mole Fractions . *ECS Meet. Abstr.* **2020**, *MA2020-02* (59), 3006–3006. https://doi.org/10.1149/ma2020-02593006mtgabs.

(45) Canongia Lopes, J. N.; Deschamps, J.; Pádua, A. A. H. Modeling Ionic Liquids Using a Systematic All-Atom Force Field. *J. Phys. Chem. B* **2004**, *108* (6), 2038–2047. https://doi.org/10.1021/jp0362133.

(46) Mains, G. J.; Nantsis, E. A.; Carper, W. R. Ab Initio Bonding, Molecular Structure, and Quadrupole Coupling Constants of Aluminum Chlorides. *J. Phys. Chem. A* **2001**, *105* (17), 4371–4378. https://doi.org/10.1021/jp004549w.

(47) Jewett, A. I.; Stelter, D.; Lambert, J.; Saladi, S. M.; Roscioni, O. M.; Ricci, M.; Autin, L.; Maritan, M.; Bashusqeh, S. M.; Keyes, T.; Dame, R. T.; Shea, J. E.; Jensen, G. J.; Goodsell, D. S. Moltemplate: A Tool for Coarse-Grained Modeling of Complex Biological Matter and Soft Condensed Matter Physics. *J. Mol. Biol.* **2021**, *433* (11), 166841. https://doi.org/10.1016/j.jmb.2021.166841.

(48) Martinez, L.; Andrade, R.; Birgin, E. G.; Martinez, J. M. Packmol: A Package for Building Initial Configurations for Molecular Dynamics Simulations. *J. Comput. Chem.* **2009**, *30*, 2157–2164. https://doi.org/10.1002/jcc.

(49) Humphrey, W.; Dalke, A.; Schulten, K. VMD: Visual Molecular Dynamics. *J. Mol. Graph.* **1996**, *14* (October 1995), 33–38.